Journal of Materials Chemistry A

ROYAL SOCIETY OF CHEMISTRY

PAPER

View Article Online
View Journal

Cite this: DOI: 10.1039/d5ta04050g

Graphene-templated hybrid Prussian blue-MXene nanocomposites for broadband photodetection with ultra-high carrier generation†

Akash Gupta,[a] Young Jun Rho,[a] Wei-Chen Lin,[bc] Dinesh Kumar Patel,[d] Chi-Te Liang,[e] Mukesh Kumar Thakur,*[f] Ilka Kriegel,[g] Francesco Di Stasio,[f] Sang Hyun Lee*[a] and Yong Il Park*[a]

A graphene template provides a unique opportunity to combine nanomaterial building blocks on its surface for versatile optoelectronic applications. Herein, a low-cost, facile, and non-toxic nanocomposite of 2D metallic MXene (MX) and Prussian blue (PB) on a graphene template is reported. The MX nanosheets are exfoliated from the MAX phase *via* HF etching and are decorated with semiconducting PB by using a novel one-step *in situ* method. This conjugation effectively anchors PB to MX, thereby enhancing the light absorption and providing a significant 19-fold increase in fluorescence quenching due to direct charge transfer. The PB@MX nanocomposite is then coated onto the graphene template to fabricate a heterostructured photodetector (PD) that exhibits enhanced photocurrent and highly sensitive broadband photodetection across the 325–808 nm range. The nanocomposite-based PD exhibits a remarkable photocurrent of 47.97 μA, a high photoresponsivity of 14 880 A W^{-1}, a detectivity of 3.72 × 10^{12} cm $Hz^{1/2}$ W^{-1}, and a normalized gain of 4.15 × 10^{-4} m^2 V^{-1} under 450 nm illumination at 31.84 μW cm^{-2} and 1 V. These values represent the best performance reported to date for this class of nanohybrids, thus highlighting the potential of this PD for real-world electronic applications.

Received 20th May 2025
Accepted 23rd July 2025

DOI: 10.1039/d5ta04050g

rsc.li/materials-a

Introduction

A photodetector (PD) is a light-sensing device that converts optical photons into electrical signals.[1] It has a wide range of applications, from agriculture to modern communication systems, and serves as a key component in various types of optical sensors.[2–6] In PD devices,[7–9] the choice of active material plays a critical role, particularly in determining the device's ability to absorb photons across specific wavelength ranges and convert them into electrical signals.[8,10–13] In recent decades, significant progress has been made in developing alternative materials that can compete with conventional silicon-based technologies, especially since the discovery of graphene.[12] Graphene can absorb a broad spectrum of wavelengths,[7–9,14] from deep ultraviolet to terahertz, with a light absorption of approximately 2.3% per layer.[7,14,15] However, due to their ultrafast charge-carrier recombination rate, graphene-based PDs typically suffer from very low responsivity (on the order of mA W^{-1})[7,9] and a high dark current, thus resulting in low detectivity and limiting their practical applications.[8,9] Nevertheless, the discovery of graphene has opened new avenues in materials science, inspiring the exploration of other two-dimensional (2D) materials such as transition metal dichalcogenides (TMDCs), which possess unique optical and electrical properties. Although numerous TMDC-based devices have been reported, they often generate relatively low photocurrents (in the nanoampere range), and their fabrication processes are time-consuming due to the size constraints of TMDC materials.[3,16,17]

In 2011, MXenes emerged as a new class of 2D materials composed of transition metal carbides and nitrides, with the general formula $M_{n+1}X_nT_x$ (where n = 1, 2, 3, or 4). These materials consist of a transition metal (M; *e.g.*, titanium), carbon and/or nitrogen (X), and various surface functional groups (T; *e.g.*, –O, –OH, and –F).[10,12,18] The MXenes exhibit unique optical and electrical properties, including high conductivity (>10^4 S cm^{-1}),[19] mechanical flexibility, tunable work functions, and chemical stability. These characteristics make the MXenes promising candidates for a wide range of

[a]School of Chemical Engineering, Chonnam National University, Gwangju 61186, Republic of Korea. E-mail: leeshyun@jnu.ac.kr; ypark@jnu.ac.kr
[b]Taiwan International Graduate Program (TIGP), Academia Sinica, Taipei 115, Taiwan
[c]Taiwan and Department of Engineering and System Science, National Tsing Hua University, Hsinchu 300, Taiwan
[d]Physikalisch-Technische Bundesanstalt (PTB), Braunschweig 38116, Germany
[e]Department of Physics, National Taiwan University, Taipei 106, Taiwan
[f]Photonic Nanomaterials, Istituto Italiano di Tecnologia, Genova 16163, Italy. E-mail: mukesh.thakur@iit.it
[g]Department of Applied Sciences and Technology, Politecnico di Torino, Torino 10129, Italy

† Electronic supplementary information (ESI) available. See DOI: https://doi.org/10.1039/d5ta04050g

applications, such as PDs,[10,18,20,21] triboelectric devices, sensors, electromagnetic interference shielding, photoelectrochemical catalysis, and optical transmission and modulation.[18,19,22,23] Although various MXene-based PD architectures, such as Mo_2CT_x,[10] ScC_zOH,[10] $Ti_3C_2T_x$/*n*-Si,[22] and Mo_2C/graphene hybrids,[10] have been investigated, PDs composed solely of MXene materials still suffer from poor photoresponse characteristics.

Prussian blue (PB) has a 3D transition metal coordination nanostructure composed of an Fe(II)–CN–Fe(III) framework and exhibits outstanding electrochemical properties, along with broad optical absorption and a semiconducting bandgap of 1.75 eV.[24,25] These attributes make PB highly versatile for applications in electrochromic devices, batteries, counter electrodes, displays, and energy storage.[24–27] Moreover, the electronic conductivity of PB can be improved, thereby enhancing its electrochemical performance, by combining it with 2D graphene oxide.[28] In particular, PB nanostructures have been utilized to increase the charge carrier density and enable charge-carrier photoexcitation, thereby significantly boosting the performance of UCNP@Au/PB-based PDs.[8] Recent studies on MXene-based heterostructured PDs have shown promising responsivity, with *R* values in the mA W^{-1} range. However, their photocurrent generation remains limited to only a few μA, and the preparation of these active materials often involves multiple steps, small-scale production, costly chemical precursors (*e.g.*, perovskites and lanthanides), limited air stability (perovskites), and specialized equipment. Hence, the process is both time-consuming and resource-intensive, which underscores the need for a more efficient approach.

To address these issues, a nanohybrid material based on PB-decorated MXene (designated as PB@MX) is developed herein *via* an *in situ* method. This synthesis strategy offers several advantages, including the elimination of additional surface modifications, extra steps, supplementary chemicals, expensive instrumentation, and extensive effort, while ensuring strong material conjugation and providing a straightforward, efficient protocol for thermal decomposition-based methods. Although MX and PB have been individually investigated for energy storage and photodetection applications,[8,21,22,29,30] to the best of the present authors' knowledge, this is the first report on the successful integration of an *in situ* synthesized PB@MX/graphene heterostructure, demonstrating enhanced optoelectronic properties and improved device performance. The PB@MX nanohybrid is well-suited for next-generation PDs, and is capable of converting more photons into electricity, thereby achieving a high photocurrent and enhanced device performance. Thus, a cost-effective, dual-terminal MX/Gr/SiO_2/Si and PB@MX/Gr/SiO_2/Si heterostructured PD device is introduced herein that achieves highly efficient photon-to-electricity conversion. In detail, MX nanosheets are synthesized *via* the hydrofluoric acid (HF) etching of Al from the MAX phase, and PB@MX nanocomposites (NCs) are produced *via* the scalable *in situ* decomposition of sodium ferrocyanide on MX to yield nanostructures with excellent dispersibility, stability, and enhanced optical properties. Comprehensive characterization confirms the NC formation and demonstrates improved visible absorption and fluorescence quenching therein, thereby suggesting efficient charge transfer from PB to MX. Finally, the MX and PB@MX photoabsorbers are coated onto graphene charge transporters on SiO_2/Si substrates with metallic contacts to develop heterostructured gate-free broadband PD devices. The NC-based PD achieves a photocurrent of 47.97 μA, with a responsivity (*R*) of 14 880 A W^{-1}, a detectivity (*D**) of 3.72×10^{12} cm $Hz^{1/2}$ W^{-1}, and a normalized gain (Γ_n) of 4.15×10^{-4} m^2 V^{-1} under 450 nm illumination at 31.84 μW cm^{-2} and 1 V. This performance is attributed to strong light–matter interactions that enhance the charge-carrier accumulation at the MX-PB interface, thereby facilitating efficient charge separation and transport through graphene and resulting in a negative photocurrent. These values mark the best reported performance for this nanohybrid PD, thereby highlighting its potential for practical electronic applications.

Results and discussion

The integrity of the as-synthesized nanomaterial, including size, shape, and elemental composition, is revealed by the transmission electron microscopy (TEM), field-emission scanning electron microscopy (FE-SEM), and energy dispersive X-ray spectroscopy (EDS) results in Fig. 1. As indicated by the low-resolution TEM image in Fig. 1a, the hydrothermally synthesized PB nanocrystals exhibit a cubic shape and are well-dispersed, with particle sizes ranging from as little as ~114 nm up to 1.1 μm (average diameter = 0.576 ± 0.22 μm), which is consistent with previous studies.[31] This variation in PB nanocrystal size may result from uncontrolled growth during synthesis. The chemical composition of the PB nanocrystals is confirmed by the EDS profile in Fig. 1b and the EDS maps in Fig. S1 of the ESI,† which indicate the presence of the elements C, O, N, and Fe, in agreement with previous work.[31]

Meanwhile, the morphology of the HF-etched 2D MXene (Ti_3C_2F, MX) nanosheet is revealed by the low-magnification top-view FE-SEM image in Fig. 1c. Here, the nanosheets exhibit multilayered, thin, sheet-like structures with lateral dimensions ranging from 3 to 15 μm. Furthermore, the elemental composition of the MX after HF etching is revealed by the EDS profile in Fig. S2a† and the EDS mappings in Fig. S3.† Here, the detection of the elements C, O, F, and Ti confirms the formation of the MX nanosheet. Notably, the absence of any Al indicates that the Al atoms are replaced by F atoms during HF treatment of the MAX phase.[32,33]

A low-magnification top-view FE-SEM image of the *in situ* synthesized PB@MX NC is presented in Fig. 1d. Here, the morphology of the individual embedded PB nanocrystals (solid red squares) and their decoration on the MX nanosheet (indicated by the yellow dotted line) is clearly observed. Notably, the sizes of the embedded PB nanocrystals (average diameter ~0.55 μm) are similar to those of the bare PB nanocrystals in Fig. 1a. The stepwise development of MX and the PB@MX NC is schematically illustrated in Fig. S4.† During synthesis, strong conjugation occurs between PB and MX. In PB, Fe^{2+} centers are coordinated with six –CN ligands, while the MX surface is terminated with –OH and –F groups. Upon interaction, some of

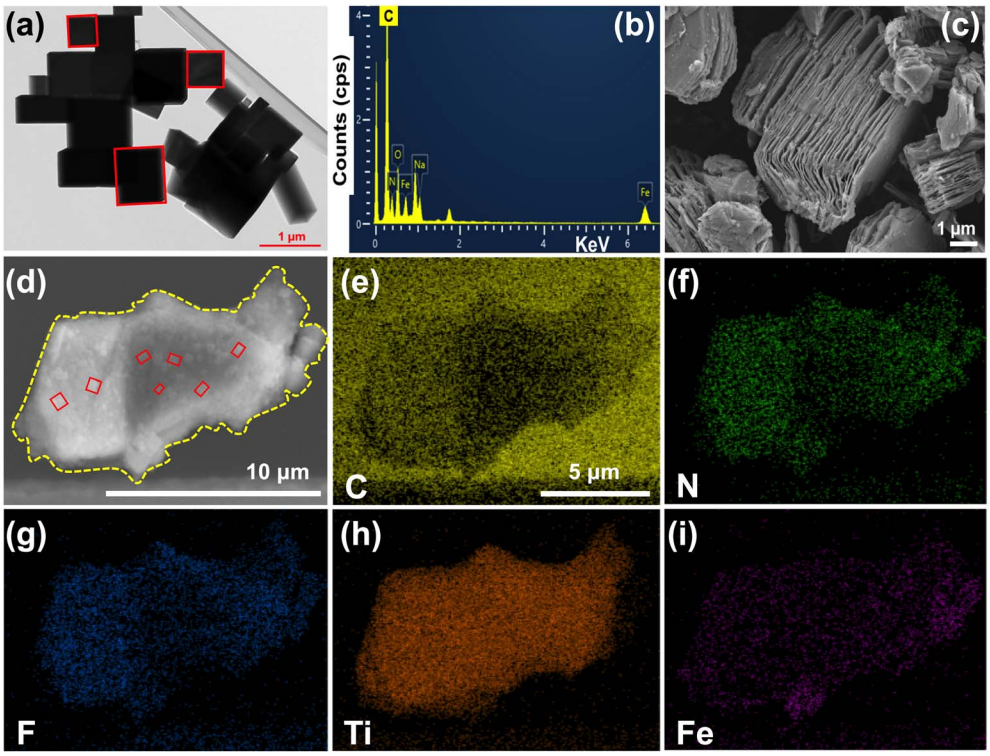

Fig. 1 (a and b) A TEM image (a) and EDS profile (b) of the PB nanocrystals. (c) An FE-SEM image of the HF-etched MX. (d–i) An FE-SEM image (d) and EDS mappings (e–i) of the PB@MX NC showing (e) C, (f) N, (g) F, (h) Ti, and (i) Fe. In part (d), the PB and MX are highlighted by solid red and dotted yellow lines, respectively.

the –CN ligands may be partially replaced by oxygen atoms from the –OH groups on MX, thus leading to the formation of covalent Fe–O–Ti linkages. The coverage of MX over each PB nanocrystal is evident in the FE-SEM image in Fig. S5.† The formation of the *in situ* PB@MX NC is further confirmed by the EDS mappings in Fig. 1e–i, along with the EDS profile in Fig. S2b.† Here, the elements C, O, N, and Fe originate from the PB nanocrystals (*c.f.* Fig. 1b), while some C and O are also derived, along with F and Ti from the MX nanosheet (*c.f.* Fig. S2a†).

To determine whether MX decoration by the PB nanocrystals occurs individually and on a large scale, or if the MX nanosheet is completely covered by the PB nanocrystals, a more detailed analysis is presented in Fig. S6.† Here, the selective area FE-SEM image and EDS analysis clearly reveal the individual PB-decorated MX nanosheets, as confirmed by the presence of all relevant chemical elements from both PB and MX. Additionally, the FE-SEM image and EDS analysis of the PB@MX NC in Fig. S7† highlight two micron-scale MX particles uniformly covered with PB nanocrystals, while the zoomed-in view in Fig. S8† reveals the coverage of the MX by many PB nanocrystals.

In addition, the chemical composition and surface electronic states of the *in situ* synthesized PB@MX NC are further elucidated by the X-ray photoelectron spectroscopy (XPS) results in Fig. S9.† There, the full XPS survey spectrum of the PB@MX NC (Fig. S9a†) confirms the presence of the elements C, O, N, Fe, F, and Ti, in agreement with the above EDS analysis. Moreover, the core-level XPS analyses in Fig. S9b–g,† indicate binding energies of 283.9–285.3 eV for the C 1s level, 530.5–531.9 eV for the O 1s level, 158.5 eV for the N 1s level, 171.7 and 173.9 eV for the Fe 2p level, 685.43 eV for the F 1s level, and 86.6 eV for the Ti 2p level.[34] Furthermore, the triplet peaks observed in the C 1s spectrum after curve fitting (Fig. S9b†) indicate the presence of C–C/C–H, C–O, and C=O/O–C–O functional groups, while the O 1s spectrum reveals the presence of $-O^-$ (532.9 eV) and O=C (531.2 eV) groups.[34,35]

The crystalline structure of the PB@MX NC and the functional groups present are further elucidated by the powder X-ray diffraction (P-XRD) and Fourier-transform infrared (FTIR) analyses in Fig. S10 and S11.† Thus, the P-XRD pattern of the pristine PB (black profile, Fig. S10†) exhibits diffraction peaks at 17.20°, 32.5°, 35°, 53.85°, and 69°, corresponding to the respective (200), (222), (400), (600), and (642) lattice planes of the face-centered cubic (fcc) crystalline phase (JCPDS 73-0687). This is consistent with the results of previous studies.[8,36,37] Meanwhile, the P-XRD spectrum of the MX (red profile, Fig. S10†) exhibits new peaks at 8.9° and 32.5°, thereby indicating the incorporation of fluorine into the $Ti_3C_2T_x$ interlayers, and a broad peak at around 39°, reflecting the removal of Al from the Ti_3AlC_2 MAX phase after HF etching. These results confirm the formation of the $Ti_3C_2F_2$-based MXene, and are consistent with previous reports.[32] Further comparison with the pristine MAX phase (Fig. S12†) reveals a shift of the (002) peak from 9.4° to 8.9°, which is indicative of an increased interlayer spacing due to exfoliation and surface termination. The

disappearance of the peak at 38.8° and the appearance of a broad peak at 39.4° further confirm successful MXene formation. Furthermore, a complementary Raman analysis reveals characteristic shifts in the vibrational bands before and after etching, thus supporting the development of 2D MX nanosheets (Fig. S13†). Finally, the XRD profile of the PB@MX NC (blue profile, Fig. S10†) displays intense, sharp diffraction peaks matching those of the individually prepared PB and MX samples, along with a few additional peaks indicating the formation of PB@MX NC with high crystallinity.

The various characteristic functional groups of the individual PB and MX are revealed by their stretching modes in the corresponding FTIR spectra (Fig. S11†). For the PB (black profile), these include O–H (3597 cm^{-1}), ≡N (2066 cm^{-1}), C═N (1607 cm^{-1}), and Fe–C (599 cm^{-1}),[8,36] while O–H (3597 cm^{-1}), C═O (1685 cm^{-1}), C–F (1079 cm^{-1}), and Ti–O (618 cm^{-1}) are observed in the MX (red profile).[32] Notably, these functional groups and their respective stretching modes are also present in the PB@MX NC (blue profile). Taken together, the above TEM, FE-SEM, EDS, XPS, P-XRD, and FTIR analyses confirm the formation of PB@MX NC from the PB and MX components.

The optical properties of the PB, MX, and PB@MX NC are revealed by the photographic images and corresponding optical absorption, fluorescence, and Raman spectra in Fig. 2. First, photographic images of colloidal solutions of the PB, MX, and PB@MX NCs dispersed in water (3 mL, 2 mg mL^{-1}) are presented in Fig. 2a. Here, it can be seen that the PB, MX and PB@MX NC solutions exhibit blueish, gray, and slightly greenish colors, respectively. Meanwhile, the optical absorption spectra of the three colloidal solutions are compared in Fig. 2b. Here, the PB (black line) exhibits an absorption minimum at 538 nm, which is consistent with previous reports.[8,36] Meanwhile, the MX nanosheets display a featureless optical absorption profile (red line), with a weak minimum at approximately 325 nm, thus confirming the metallic nature of the HF-etched MX, in agreement with previous reports.[38,39] The featureless absorption of the MX nanosheets in the long wavelength (450–900 nm) range is attributed to strong light scattering. By contrast, the PB@MX NCs (blue profile) exhibit significantly enhanced and well-defined absorption peaks at 310, 478, and 565 nm.[8] The modified optical absorption behavior of the PB@MX NCs compared to the pristine components can be attributed to light–matter interactions, which facilitate the transfer and accumulation of charge carriers at the interface between the metallic MX and semiconducting PB domains within the NC.

The Raman spectrum of the monolayer graphene on an SiO_2/Si substrate is shown in Fig. 2c, along with an inset showing an optical microscope image with the boundary between the Gr/SiO_2/Si and SiO_2/Si highlighted. The spectrum in Fig. 2c exhibits all the characteristics of the main Raman bands, including the G and 2D peaks at 1585 cm^{-1} and 1683 cm^{-1}, respectively, along

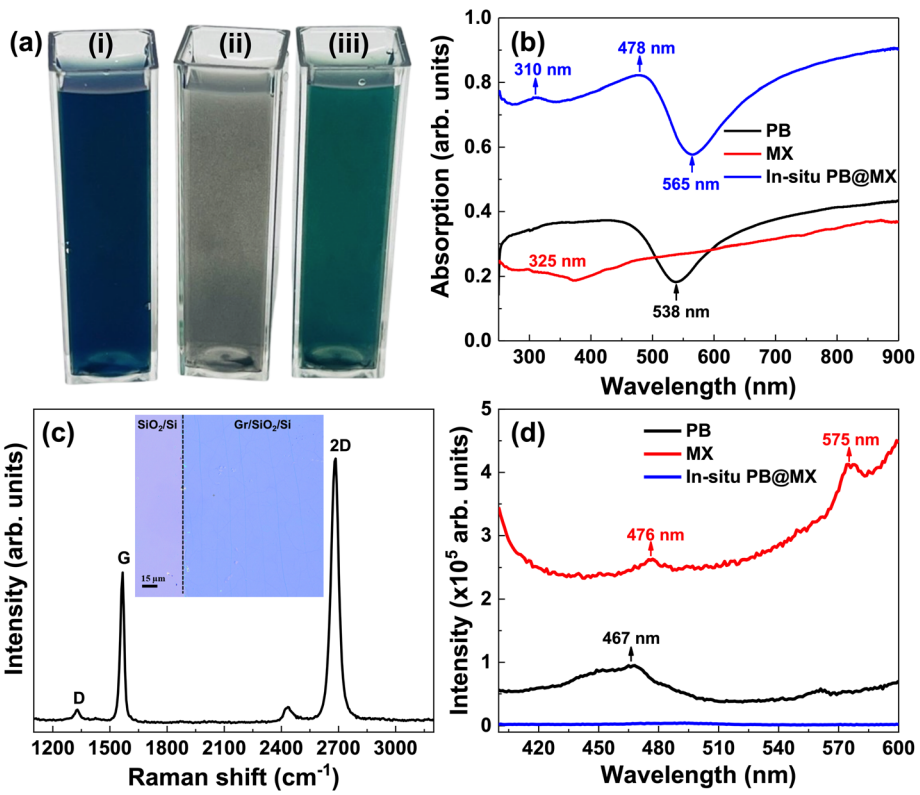

Fig. 2 (a) Photographic images of (i) the PB, (ii) the MX, and (iii) the PB@MX NC dispersed in water in quartz cuvettes. (b) The optical absorption spectra of the three solutions. (c) The Raman spectrum of monolayer graphene on an SiO_2/Si substrate, with an inset showing an optical image of the sample. (d) The fluorescence emission spectra of the MX, PB, and PB@MX NC dispersions under 350-nm UV excitation.

with a small D mode at 1328 cm^{-1} due to substrate strain. These results confirm the presence of monolayer graphene and are consistent with previous studies.[9,14,40,41] The monolayer graphene, with its high carrier mobility, plays a crucial role in PD applications by functioning as a charge transport material.[7–9,14] Meanwhile, the Raman spectra of the MX, PB@MX, and PB@MX/Gr monolayers on SiO_2/Si substrates are presented, along with a detailed explanation, in Fig. S14.† These results confirm the successful formation of the PB@MX/Gr heterostructure, as indicated by the presence of characteristic peaks corresponding to all constituent elements and interactions between the materials.

The fluorescence spectra of the three dispersions under 350 nm excitation are shown in Fig. 2d. Here, the weak fluorescence spectrum of the PB (black line) exhibits a peak with a maximum intensity at 467 nm, which likely originates from electronic transitions from the Fe^{2+} state to the Fe^{3+} state and subsequent relaxation, thus resulting in visible emission.[42] Meanwhile, the fluorescence emission spectrum of MX exhibits two peaks at 476 and 575 nm, which are attributed to a minimal TiO_2 residue remaining after HF etching of the MAX phase.[41] Notably, the emission spectrum of the PB@MX NC exhibits ~19-fold quenching, thus resulting in negligible intensity due to light–matter interactions that facilitate efficient charge transfer from the PB to the metallic MX. A similar trend is observed for the solid-state samples on SiO_2/Si substrates in Fig. S15,† where more substantial fluorescence quenching is observed in the PB@MX NC/Gr/SiO_2/Si. These results suggest efficient charge transfer between the PB@MX NC and graphene, as evidenced by the fluorescence quenching behavior and corresponding quenching efficiency. The calculated quenching efficiencies are 74.2% and 96.5% for the PB@MX/SiO_2/Si and PB@MX/Gr/SiO_2/Si, respectively, thus confirming a highly efficient charge transfer process. These findings support the proposed charge transfer mechanism and are consistent with the enhanced photoresponse observed in the device.

It is important to note that the development of PB@MX NC is not directly assisted by HF etching; HF is used solely for preparing MX nanosheets from the MAX phase. The resulting –F surface terminations influence PB growth by modifying the nucleation behavior and tuning the local electronic environment. This leads to red-shifted absorption peaks and significant fluorescence quenching, thus confirming efficient charge transfer and an enhanced optoelectronic performance.

Here, PD devices were fabricated based on MX/Gr/SiO_2/Si and PB@MX/Gr/SiO_2/Si structures, as shown schematically in Fig. 3a and b. First, a monolayer of CVD-grown graphene was transferred onto an SiO_2/Si substrate to serve as the channel material, after which Ti/Au source and drain electrodes were deposited, with the Ti acting as an adhesive layer (Fig. S16†). The photoactive PB@MX NC layer was then spin-coated onto this structure and illuminated under various light excitations, as depicted in Fig. 3b. An optical microscope image of the as-fabricated device prior to PB@MX deposition is presented in Fig. 3c, clearly revealing the uniform graphene monolayer between the Ti/Au electrodes on the SiO_2/Si substrate. Here, the

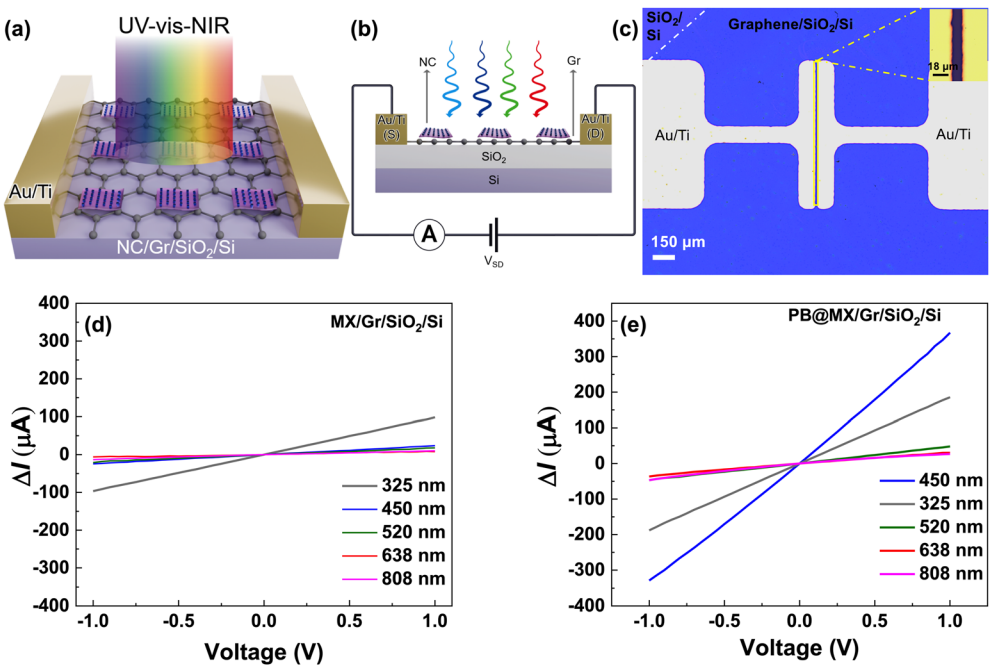

Fig. 3 (a and b) 3D (a) and planar (b) schematic illustrations of the PD based on the PB@MX/Gr/SiO_2/Si heterostructure. The source and drain electrodes connected *via* a voltmeter and ammeter are depicted in the planar side view. (c) An optical microscope image of the actual PD device before material spin coating, showing the SiO_2/Si substrate, Au/Ti electrodes, and a uniform single layer of graphene, along with an inset highlighting the device's active area. (d and e) Plots of the photocurrent (ΔI) as a function of source-drain voltage ($V_{DS} = -1$ V to +1 V) for (d) the MX/Gr/SiO_2/Si- and (e) the PB@MX/Gr/SiO_2/Si-based heterostructured PDs under illumination, with a power density of 1282 μW cm^{-2} in the wavelength range of 325–638 nm and a power density of 31 847 μW cm^{-2} at 808 nm.

inset shows the device's active area of 10 123 μm^2, with a device length and width of 955 μm and 10.6 μm, respectively. The details of the step-by-step device fabrication procedure are provided in the Experimental section and shown schematically in Fig. S16.†

To analyze the effects of the pristine graphene, MX/Gr, and PB@MX/Gr on the dark current, the *I–V* (dark) characteristics are shown in Fig. S17c and d,† while an optical image of the Gr/SiO_2/Si before and after coating with PB@MX are presented in Fig. S17a and b.† Thus, the dark current of both the MX/Gr and PB@MX/Gr remains nearly unchanged compared to that of the pristine graphene, thereby indicating that the crystallinity of each material is preserved. This also confirms that the graphene functions as a channel material without interfering with MX and PB@MX. As a control, a standalone MXene-based device was also fabricated, as shown in Fig. S17d,† where the drain current is in the order of nA. Meanwhile, the *I–V* characteristics of the MX/Gr/SiO_2/Si and PB@MX/Gr/SiO_2/Si devices under various drain-source voltage (V_{DS}) values of −1 V to +1 V and various illumination wavelengths are shown in Fig. 3d and e. Here, a fixed power density of 1282 μW cm^{-2} is used for the broadband region (325–638 nm), while a power density of 31 847 μW cm^{-2} is used for the 808 nm laser. The results indicate that the change in photocurrent (ΔI = light current (I_L) − dark current (I_D)) scales linearly with the applied bias voltage under identical conditions, thus confirming the ohmic nature of the Au/Ti contacts. This is consistent with several previous studies on hybrid PDs.[7–9,14,40] At a V_{DS} of 1 V and a power density of 1282 μW cm^{-2}, the MX/Gr/SiO_2/Si PD exhibits photocurrent values ranging from 98.92 μA at 325 nm to 7.9 μA at 638 nm (Fig. 3d). At a power density of 31 847 μW cm^{-2}, however, a photocurrent of 10.38 μA is obtained at 808 nm for the same device. The enhanced photocurrent at 325 nm correlates with the strong UV absorption peak of MX observed in Fig. 2b. By comparison, the PB@MX/Gr/SiO_2/Si device demonstrates superior performance, achieving its maximum photocurrent of 367 μA under 450 nm illumination at a V_{DS} of 1 V and a power density of 1282 μW cm^{-2} (Fig. 3e). Under identical conditions, this device generates photocurrents of 186, 50, and 30 μA at wavelengths of 325, 520, and 638 nm, respectively. This enhanced photoresponse of the PB@MX NC-based device compared to the MX-only device stems from efficient light–matter interactions at the PB-MX interface, which lead to enhanced charge-carrier accumulation.

The dynamic photoresponse (*I–t*) characteristics of the MX/Gr/SiO_2/Si PD (black) and PB@MX/Gr/SiO_2/Si PD (red) at illumination wavelengths of 325, 450, 520, 638, and 808 nm are presented in Fig. 4a–e, respectively. Here, each panel represents multiple ON/OFF switching cycles, where "ON" represents light illumination of the device and "OFF" indicates no illumination, with the response being measured at a fixed bias voltage (V_{DS} = 1 V) and a constant power density of 1282 μW cm^{-2} in the 325–638 nm range and 31 847 μW cm^{-2} at 808 nm. These results demonstrate that both devices exhibit reproducible and stable switching behavior under periodic broadband illumination. Moreover, both devices exhibit negative photocurrent behavior; this observation indicates that when light is incident on the device, the photocurrent curve shifts in a negative direction, which suggests that electrons are transferred from PB@MX to

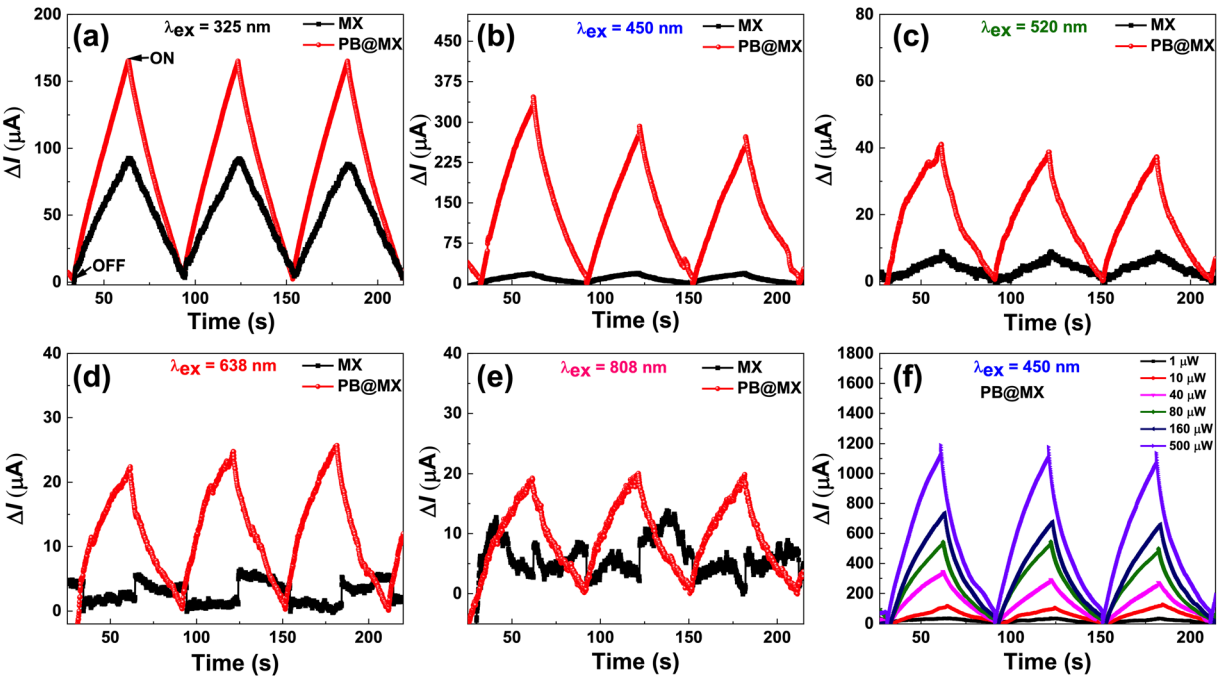

Fig. 4 The multicycle dynamic photoresponses of the MX/Gr/SiO_2/Si (black) and PB@MX/Gr/SiO_2/Si (red) heterostructured PDs under illuminating wavelengths of (a) 325 nm, (b) 450 nm, (c) 520 nm, (d) 638 nm, and (e) 808 nm at an applied bias voltage of 1 V and identical power densities of 1282 μW cm^{-2} in the 325–638 nm range and 31 847 μW cm^{-2} at 808 nm. (f) The power-dependent multicycle dynamic photoresponse of the PB@MX/Gr/SiO_2/Si-based PD at various incident powers under an illuminating wavelength of 450 nm at 1 V of V_{DS}.

graphene, thus resulting in a negative photocurrent.[43] This behavior can be understood by considering the work function of graphene and the ionization energy of PB@MX. According to the published literature, the work function of graphene is approximately 4.4 eV,[44] while the ionization energy of PB@MX ranges from 5.7 to 6 eV, with the individual ionization energies of PB and MX being 5.4 and 6.2 eV, respectively.[25,45,46] As more photons from the excitation light are incident on the material, an increasing number of photogenerated electrons are transferred from PB@MX to graphene at an accelerated rate. This process ultimately leads to a rise in the Fermi energy level of graphene. This interpretation is further supported by the PL spectra of the PB@MX and PB@MX/graphene flakes in Fig. S15,† where a significant quenching effect is observed in the latter. This quenching confirms effective charge transfer from PB@MX to graphene upon light illumination.

The considerable p-type doping of the CVD-grown graphene results in a high concentration of positive charge carriers (holes). When the MX/Gr and PB@MX/Gr heterostructures are exposed to illumination, the photogenerated electrons accumulate and interact with the p-type charge carriers, which partially neutralizes the p-type doping effect and ultimately results in a negative photoresponse.[43]

The above results indicate that the MX/Gr-based PD exhibits a maximum photocurrent of 94.14 μA under 325 nm illumination at a power density of 1282 μW cm^{-2}, followed by 24.56 μA at 450 nm under the same conditions. The photocurrent significantly decreases to 9.6, 6.6, and 10.6 μA at illumination wavelengths of 520, 638, and 808 nm, respectively. By contrast, the as-synthesized PB@MX NC-based device exhibits superior photodetection capabilities, with a record photocurrent of 350 μA under 450 nm illumination at 1282 μW cm^{-2}, which represents a 14-fold enhancement compared to the MX/Gr-based device under identical conditions. The PB@MX-based device also exhibits enhanced photocurrents of 167, 41.97, and 26.11 μA at 325, 520, and 638 nm, respectively, which correspond to enhancement factors of 1.7, 4.3, and 3.9 times compared to the MX/Gr-based device. This significant improvement in photocurrent is attributed to enhanced photoabsorption and substantial charge accumulation in the PB@MX NC, as evidenced by the absorption spectra in Fig. 2b. Under NIR (808 nm, 31 847 μW cm^{-2}) illumination, however, the PB@MX/Gr demonstrates low sensitivity, with a photocurrent of 21.91 μA, which is only twice that of the MX/Gr-based device.

Notably, in a previous study by the present research group, the bare CVD-grown graphene-based device exhibited a negligible photoresponse (ΔI <0.5 μA) even at an ~22 000 times higher power density of 716 mW cm^{-2} under visible laser illumination at 1 V bias.[9] This is consistent with the low optical absorption of graphene, at 2.3% per layer,[14,47] and confirms that the enhanced photocurrent of the PB@MX/Gr device stems from the active NC layer, rather than the underlying device structure. Moreover, as shown in Fig. 4e, the PB@MX/Gr PD demonstrates enhanced sensitivity to blue light (450 nm), detecting an optical power as low as 1 μW (31.84 μW cm^{-2}) and generating a remarkable photocurrent of 47.97 μA. This represents an improved performance compared to previously-reported devices based on similar materials.[8,20,48–53] The PB@MX/Gr-based PD exhibits conventional semiconductor behavior, wherein the photocurrent increases proportionally with the power density of the 450 nm laser illumination.[3] In addition, the photocurrent responses of the MX/Gr- and PB@MX/Gr-based devices under various power densities and broadband laser illuminations are compared in Fig. S18–S20.†

The functional stability and reproducibility of the PB@MX/Gr-based device during eleven consecutive ON/OFF cycles under 450 nm laser illumination (80 μW, V_{DS} = 1 V) is demonstrated in Fig. S21a.† Moreover, the extended illumination tests under 450 nm laser illumination for 115 s in Fig. S21b† reveal a continuous increase in photocurrent without saturation, thereby indicating the accumulation of charge carriers and their continuous transport to the electrodes. Meanwhile, the reproducibility of the PB@MX coating is confirmed by consistent photocurrent generation across four devices under identical illumination conditions in Fig. S22.† As a key parameter for PD applications, the stability of both the PB@MX material and the PB@MX-based PD device was further evaluated by monitoring its performance over six months of operation. The dynamic photocurrent measurements under similar conditions in Fig. S23d† show that the device retains over 90% of its initial performance even after six months, thereby demonstrating excellent stability. This is further supported by the unchanged color of the PB@MX NC solution in liquid form and the preserved structural integrity, as shown in Fig. S23a–c.† Moreover, the optimized PD device maintains its ability to detect signals from a camera flash and a green laser pointer even after 191 days under a 1 V bias (Fig. S24†), exhibiting a stable and reproducible high photocurrent response.

For further investigation of the device mechanism and quantification of the trap states, the power-dependent photocurrent is analyzed using the standard power law, *i.e.*, $I = bP^{\alpha}$, where α is a dimensionless exponent that characterizes the trap states for the minority carriers in the photodetection system, b is a detector-specific parameter, and P denotes the incident light power.[8,9] An α value of 1 indicates a trap-free device exhibiting the photoconductive effect, where the responsivity remains constant with illumination power.[3] When α < 1, the device contains trap states, thus resulting in a sub-linear dependence of responsivity on the power density, which is known as the photogating effect.[3] In the present work, the α values were determined by plotting photocurrent *versus* laser power density on a log–log scale at both 450 and 638 nm wavelengths for the MX/Gr- and PB@MX/Gr-based devices, as shown in Fig. S25a and b.† This analysis reveals the presence of trap states in both devices, with the PB@MX/Gr-based device showing significantly fewer trap states under 638 nm illumination ($\alpha \approx 0.62$) compared to the MX/Gr device ($\alpha \approx 0.3$). However, under 450 nm illumination, the PB@MX/Gr- and MX/Gr-based devices exhibit comparable trap state densities of $\alpha \approx$ 0.46 and 0.79, respectively. These sub-unity α values indicate that the photogating effect dominates the functional mechanism of the device.

The efficient light-to-current conversion mechanism of the hybrid PD is illustrated by the energy band diagram in Fig. 5,

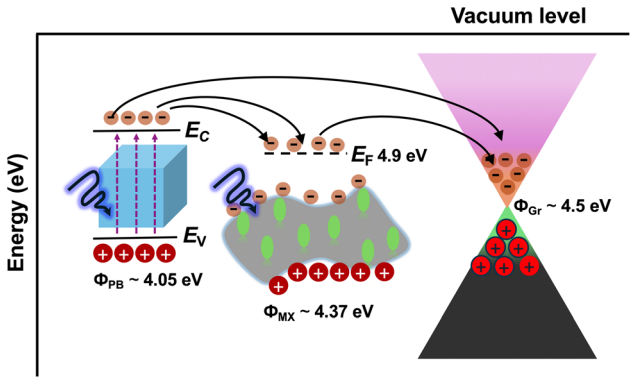

Fig. 5 An electronic band diagram illustrating the generation of a negative photocurrent in the PB@MX/Gr/SiO_2/Si-based PD device, indicating the valence (E_V) and conduction (E_C) bands of both PB and p-type CVD-grown graphene (Gr), along with the Fermi level (E_F) of MX. Here, Φ_{PB}, Φ_{MX}, and Φ_{Gr} represent the work functions of PB, MX, and Gr, respectively. The solid black arrows indicate charge-carrier transfer from the NC to Gr, while the + and − symbols denote holes and electrons, respectively.

which shows the valence (E_v) and conduction (E_c) bands of PB, the Fermi level (E_F) of MX, and the characteristic Dirac cone of the p-type CVD-grown graphene. The work function (Φ) values for PB, MX, and graphene are approximately 4.05, 4.37, and 4.5 eV, respectively.[8,22,47] Upon illumination, the PB@MX NC absorbs incident photons, thus generating electron–hole pairs. This strong photoresponse arises from the presence of trap states ($\alpha < 1$) at the PB-MX interface (Fig. S25†) and enhanced light absorption (Fig. 2b), both of which promote efficient light–matter interactions and result in a continuous, unsaturated increase in photocurrent. Surface static charge measurements further support the dense accumulation of photoexcited electrons in the PB@MX NC, revealing a negative surface potential of approximately −1005 V (Fig. S26†). Initially, the excited electrons become trapped in the interface trap states within the PB@MX NC. Due to the favorable energy band alignment, these electrons are subsequently transferred from the conduction band of the PB to MX, and then to graphene, which acts as an effective electron acceptor owing to its relatively lower Fermi level. This sequential migration from PB to MX to graphene not only facilitates directional charge-carrier transport but also promotes effective charge separation, with holes remaining in the PB@MX region. The high electrical conductivity of graphene ensures rapid and efficient electron collection, thereby enhancing the photocurrent generation. Overall, this mechanism stabilizes the charge-separated state, thereby suppressing charge recombination, and significantly improves the PD performance by enabling efficient photocharge extraction.[8,14,43,47]

Finally, to facilitate comparison with other available devices, the key parameters of the two PD devices are evaluated, including the photoresponsivity (R), detectivity (D^*), and normalized gain (Γ_n), using the standard formulas given here as eqn (1)–(3), respectively:

$$R = \frac{\Delta I(A)}{P} \quad (1)$$

where ΔI is the photocurrent, A is the active area of the device, and P is the applied power

$$D^* = \frac{R\sqrt{A}}{\sqrt{2eI_D}} \quad (2)$$

where e is the electronic charge, I_D is the dark current, and R is obtained from eqn (1), and

$$\Gamma_n = \frac{hv}{e}\frac{\Delta I}{\eta P}\frac{l^2}{V} \quad (3)$$

where hv is the photon energy (calculated as 1240/wavelength (nm)), l is the device channel length, η is the quantum efficiency ($\eta = 1$), and V is the bias (1 V).

The estimated R values of the MX/Gr/SiO_2/Si- and PB@MX NC/Gr/SiO_2/Si-based PD devices under 325, 450, 520, 638, and 808 nm illumination at a fixed power density of 1282 μW cm^{-2} and a V_{DS} of 1 V are shown, along with that obtained at 808 nm and a power density of 31 847 μW cm^{-2}, in Fig. 6a. Under 450 and 638 nm excitation, the PB@MX NC-based device exhibits maximum and minimum responsivity values of 2714.1 and 26.1 A W^{-1}, respectively, which are approximately 14 and 3.9 times higher than those of the MX/Gr/SiO_2/Si-based device (190.45 and 6.69 A W^{-1}, respectively). The PB@MX NC-based device exhibits a significantly enhanced sensitivity to 450 nm illumination, thereby generating a high photocurrent. This is further demonstrated in Fig. 6b, where the maximum R values of the PB@MX NC-based device are examined under various powers at 450 nm illumination. Here, a maximum R value of 14 880 A W^{-1} is observed at the lowest possible power of 1 μW (31.8 μW cm^{-2}). The trend in the R values under various laser powers is further highlighted by the magnified view in the inset of Fig. 6b. Here, a notable decrease is observed in the estimated R value with the increase in laser power, which can be attributed to the non-linear scaling of photocurrent with power (Fig. 4e). When this non-linear photocurrent behavior is substituted into eqn (1), a consistent reduction in R value is obtained. This is consistent with the results of previous studies on graphene-based PD devices.[9,14,35] Under 808 nm illumination, the PB@MX NC-based device exhibits a low R value of 6.8 A W^{-1}, which is approximately twice that of the MX/Gr/SiO_2/Si-based device (3.28 A W^{-1}). The calculated power-dependent R values of the PB@MX/Gr/SiO_2/Si-based device under 450 nm laser illumination and an applied bias of 1 V are listed, along with the corresponding D^* and Γ_n values, in Table S1.†

The D^* values obtained from eqn (2) can be used to assess the sensitivity of the PD device for the detection of low-power light signals and its ability to convert them into electrical signals. The dark current values of various PD devices are shown in Fig. S27,† where the device exhibits an average I_D of 5009 μA, based on the I–V characteristics. The calculated D^* values for the MX/Gr/SiO_2/Si- and PB@MX/Gr/SiO_2/Si-based PD devices under various broadband illuminations and a fixed bias of 1 V are plotted in Fig. 6c, while the inset shows the calculated D^* values under various power densities with a fixed wavelength of

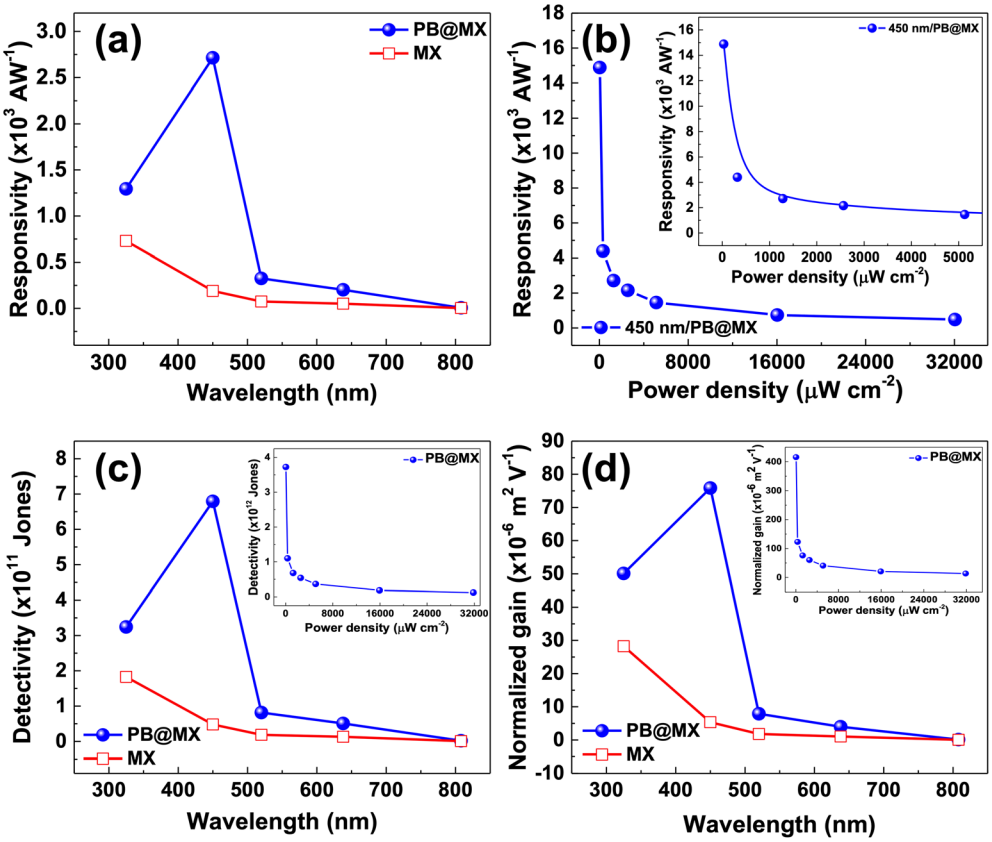

Fig. 6 (a) The wavelength-dependent photoresponsivity (R) of the MX/Gr/SiO_2/Si- and PB@MX/Gr/SiO_2/Si-based PDs at a fixed power density of 1282 μW cm^{-2} (325–638 nm) and 31 847 μW cm^{-2} (808 nm) and a V_{DS} of 1 V. (b) The photoresponsivity of the PB@MX/Gr/SiO_2/Si-based PD under 450 nm illumination at various power densities. The inset in (b) shows magnified R values under lower power densities. (c and d) The wavelength-dependent detectivity (c) and normalized gain (d) of the two PDs at a fixed power density of 1282 μW cm^{-2} (325–638 nm) and 31 847 μW cm^{-2} (808 nm), and a V_{DS} of 1 V, along with insets showing the power-density dependent detectivity (c) and normalized gain (d) of the PB@MX/Gr/SiO_2/Si-based PD under 450 nm illumination.

450 nm and the same bias. Thus, at a power density of 1282 μW cm^{-2}, the PB@MX/Gr/SiO_2/Si-based device achieves a maximum D^* of 6.79 × 10^{11} cm Hz$^{1/2}$ W^{-1} under 450 nm illumination, which is significantly higher than that of the MX/Gr/SiO_2/Si-based PD device (4.76 × 10^{10} cm Hz$^{1/2}$ W^{-1}). Consistently with the abovementioned trend in R values, the PB@MX/Gr/SiO_2/Si-based device exhibits the highest D^* value of 3.72 × 10^{12} cm Hz$^{1/2}$ W^{-1} at the lowest power of 31.84 μW cm^{-2} (inset, Fig. 6c) and a decrease in D^* is observed with the increase in illumination power. This is reasonable, as R is also a factor in calculating D^*.

Meanwhile, the normalized gain parameter (Γ_n), as calculated using eqn (3), makes it possible to compare the performance of the as-fabricated PD with that of previously-published PD devices despite differences in device architecture, size, or active area. First, the estimated photocurrent gain $\left(\Gamma = \frac{hv}{e}\frac{\Delta I}{\eta P}\right)$ is plotted as a function of wavelength, and as a function of power density at a fixed wavelength of 450 nm, for the PB@MX- and MX-based devices in Fig. S28.† The results indicate that the PB@MX-based PD achieves the highest Γ value of 41 079 at 31.84 μW cm^{-2} and 450 nm. The variations in the estimated Γ_n values for the PB@MX- and MX-based devices under broadband laser illumination at a fixed power density of 1282 μW cm^{-2} (V_{DS} = 1 V) are shown in Fig. 4d, while the inset shows the variation in Γ_n for the PB@MX-based device under 450 nm illumination at various power levels. Thus, at 450 nm and 1282 μW cm^{-2}, the PB@MX-based device exhibits a Γ_n

Table 1 The calculated photoresponsivity (R), detectivity (D^*), and normalized gain (Γ_n) values for the PB@MX- and MX-based PD devices under 325, 450, 520, 638, and 808 nm illumination at a fixed power density of 1282 μW cm^{-2} (325–638 nm) and 31 847 μW cm^{-2} (808 nm), and V_{DS} = 1 V

	R (A W^{-1})		D^* (×10^{11} cm Hz$^{1/2}$ W^{-1})		Γ_n (×10^{-6} m^2 V^{-1})	
λ (nm)	MX	PB@MX	MX	PB@MX	MX	PB@MX
325	730	1295	1.82	3.24	20.82	50.11
450	190.4	2714.1	0.47	6.79	5.32	70.58
520	74.4	325.4	0.18	0.88	1.80	7.87
638	51.8	202.4	0.12	0.5	1.02	3.99
808	3.28	6.8	0.017	0.82	0.051	0.105

Table 2 A comparison of the estimated optoelectrical device performances of MXene and its hybrid-based PDs, including the present work[a]

Material	V_{DS} (V)	Power	ΔI	R (A W^{-1})	D^* ($\times 10^{12}$ cm Hz$^{1/2}$ W^{-1})	λ (nm)	Ref.
Mo_2CT_x	1	5×10^{-4} W cm^{-2}	~1 μA	9	0.47	660	51
Ti_3C_2/Si	0	0.24 μW	~0.2 μA	0.402	20	900	54
$WS_2/Ti_3C_2T_x$	—	170 μW cm^{-2}	120 nA	0.003	0.00059	700	48
ZnO QDs/$Ti_3C_2T_x$	10	1.72 mW cm^{-2}	~8 μA	0.42	0.71	350	55
V_2CT_x–TiO_2	0	65 mW cm^{-2}	~1.2 μA	0.028	0.12	340	56
$Ti_3C_2T_x$-GaN	5	0.3 μW	—	64.6	1.93	405	57
Nb_2CT_x/AlGaN	0	600 μW cm^{-2}	—	0.101	0.012	254	50
$MAPbI_3$–$Ti_3C_2T_x$	2	20 μW cm^{-2}	0.8 μA	1.7	0.7	525	58
$CsPbBr_3$–$Ti_3C_2T_x$	10	7.07 mW mm^{-2}	5.6 μA	0.044	0.00064	450	20
$ReS_2/Ti_3C_2T_x$	2	0.25 mW cm^{-2}	—	40.8	1.07	Visible	49
$Ti_3C_2T_x$/GaAs	0	4.5 μW cm^{-2}	0.1 μA	1.46	12.3	650	52
$Ti_3C_2T_x$/PbS QD	0	19.6 μW cm^{-2}	—	0.81	92	808	21
$Ti_3C_2T_x/MoS_2$	1	1.04 mW cm^{-2}	1.6 nA	20.67	5.39	520	53
UCNP@Au/PB/EG	1	318 nW cm^{-2}	135 nA	2.9×10^5	105	432	8
$Ti_3C_2T_x$ (MX)	1	1282 μW cm^{-2}	24.56 μA	190.4	0.047	450	This work
In situ PB@MX	1	31.8 μW cm^{-2}	47.97 μA	14 880	3.72	450	This work

[a] R = photoresponsivity; ΔI = photocurrent; D^* = detectivity.

value of 7.58×10^{-5} m^2 V^{-1}, compared to 5.32×10^{-6} m^2 V^{-1} for the MX-based device (main panel, Fig. 6d). However, the PB@MX-based device exhibits its highest Γ_n value of 4.15×10^{-4} m^2 V^{-1} at the lowest power of 1 μW (31.84 μW cm^{-2}; inset, Fig. 6d), after which the estimated Γ_n decreases with the increase in laser power density; *i.e.*, the same trend is observed as for R (Fig. 6a and b) and D^* (Fig. 6c). The step-by-step calculations of all device parameters, including R, D^*, Γ, and Γ_n, are provided in Section CS1 of the ESI,† and the numerical results for both devices are summarized in Tables 1 and S1.†

In brief, the above results indicate that the PB@MX-based PD device achieves a high photocurrent of 47.97 μA, along with a photoresponsivity of 14 880 A W^{-1}, a detectivity of 3.72×10^{12} cm Hz$^{1/2}$ W^{-1}, and a normalized gain of 4.15×10^{-4} m^2 V^{-1} under 450 nm laser illumination with a power density of 31.84 μW cm^{-2} and an applied bias voltage of 1 V. The comparison with previously-published results for similar materials in Table 2 clearly demonstrates the superior performance of the as-fabricated device.

In addition, the response time (τ) is a critical parameter that characterizes the speed of the PD's photoresponse under illumination. This parameter can be estimated by using a well-established method, and provides insights into how quickly the device responds to changes in light intensity.[3] The response time is divided into rise (τ_{rise}) and fall (τ_{fall}) times, which are determined from a single dynamic photoresponse cycle such as that shown Fig. S29.† These times are calculated as the intervals between 10% and 90% of the maximum saturated photocurrent during the laser's OFF and ON states.[9,14,35,59] The results in Fig. S29† were obtained under 325 and 450 nm illumination at a power density of 2547 μW cm^{-2} and under 808 nm illumination at 159.2 mW cm^{-2}, with a V_{DS} of 1 V. Thus, under 325 and 450 nm laser illumination (Fig. S29a, b, e, and f†), both devices exhibit significantly slow rise and fall times of 23–27 s. This slow response is attributed to the sluggish extraction of trapped photoexcited electrons at the MX and PB interfaces with graphene, which results from the accumulation of trap states at these interfaces. These trap states act as localized energy levels that temporarily immobilize photogenerated electrons, delaying their transfer to graphene and consequently slowing the overall charge extraction process. This behavior leads to a prolonged response time. This explanation is further supported by the power-law dependence, where the α value ranges from 0.3 to 0.7, thus indicating the presence of trap states and suggesting that the device operation is primarily governed by the photogating effect.[3,60] However, this limitation can potentially be overcome by reducing the trap density and enhancing the interfacial charge transfer. Notably, under 808 nm illumination at 159.2 mW cm^{-2}, the MX-based device (Fig. S29c and d†) shows very rapid response times (τ_{rise} = 86 ms and τ_{fall} = 175 ms). This is due to the influence of the metallic surface plasmon of MX in the NIR spectral region,[12,61,62] which provides fast extraction of the few available accumulated electrons (low absorption; Fig. 2b) to the graphene and, hence, fast transport to the electrodes.

Conclusions

Herein, a Prussian blue decorated 2D transition metal-based MXene nanocomposite (PB@MX NC) was successfully synthesized *via* a one-step, *in situ* thermal decomposition method in an acidic medium at 70 °C. During this process, the sodium ferrocyanide precursor decomposed on the HF-etched MX nanosheets. The resulting PB@MX NC exhibited significant fluorescence quenching compared to the bare PB, which was due to the excellent charge-carrier separation and transfer into graphene under the applied voltage. The as-fabricated PD devices showcased a remarkable synergistic boost in photocurrent, delivering highly sensitive broadband photodetection across the range of 325–638 nm. As a result, the PB@MX-based PD achieved a record high photocurrent (ΔI) of 47.97 μA, along with exceptional photoresponsivity (R = 14 880 A W^{-1}),

detectivity ($D^* = 3.72 \times 10^{12}$ cm $Hz^{1/2}$ W^{-1}), and normalized gain ($\Gamma_n = 4.15 \times 10^{-4}$ m^2 V^{-1}) under 450 nm illumination at a power density of 31.84 μW cm^{-2} and a bias of 1 V. This outstanding performance is attributed to the presence of strong light–matter interactions that boost the photoexcited charge carrier accumulation at the interface between metallic MX and the semiconducting PB. By contrast, the MX-based device (without PB) was unable to detect light under these conditions. With a significantly higher power density of 1282 μW cm^{-2}, however, the MX-based PD achieved a ΔI of 24.56 μA, an R value of 190.45 A W^{-1}, a D^* of 4.76×10^{10} cm $Hz^{1/2}$ W^{-1}, and a Γ_n of 5.32×10^{-6} m^2 V^{-1} under 450 nm at the same bias.

Experimental

Materials

Sodium ferrocyanide ($Na_4Fe(CN)_6$, 99%) and hydrofluoric acid (HF; 48%) were purchased from Sigma-Aldrich (USA). Hydrochloric acid (HCl, 35%) was purchased from Daejung (South Korea). The titanium (Ti) based MAX powder (Ti_3AlC_2, 98.8%) was purchased from InnoMXene, Korea. The copper etchant iron(III) chloride ($FeCl_3$) was obtained from Alfa Aesar. All chemicals were of analytical grade and were utilized as received, without any additional purification or alteration. Graphene on copper (Gr/Cu) was purchased from Graphenea, Spain (batch no: F345030). The SiO_2/Si substrate was purchased from Osilla.

Preparation of the MXene nanosheet

The 2D transition metal-based MXene (MX) nanosheets were prepared using a standard method, which involved HF etching of the MAX phase in a controlled reaction vessel.[63,64] In this process, 500 mg of MAX powder was placed in a 100 mL low-pressure digestion vessel, and 12 mL of HF solution was very slowly added dropwise to facilitate the removal of Al layers from the MAX phase. The mixture was then gently stirred using a magnetic stirrer at 300 rpm and 28 °C for 24 h to result in the formation of MXene. After etching, the reaction mixture was washed several times with deionized (DI) water and centrifuged at 15 000 rpm for 12 min. This washing process was repeated eight times, until the solution reached a neutral pH of 7. The final MXene precipitate was dried overnight in an oven at 65 °C and stored in a glass vial for further use.

Preparation of the PB nanocrystals

The PB nanocrystals were synthesized *via* the temperature-assisted decomposition of sodium ferrocyanide with slight modifications.[28,35] In brief, 40 mM of sodium ferrocyanide was dissolved in 110 mL of distilled water in a 200 mL glass flask and stirred at 55 rad s^{-1} for 10 m. Next, 1 mL of HCl was gradually added to the mixture, which was then heated at 62 °C for 4 h with constant stirring. After allowing the solution to cool to room temperature, the resulting PB nanocrystals were washed three times with ethanol and then dried overnight in a vacuum oven at 70 °C for further use.

In situ preparation of PB@MX NC

The MXene-decorated PB NC was prepared using a similar method to the synthesis of PB alone. In this synthesis, 40 mM of sodium ferrocyanide was added to 102 mL of distilled water in a 200 mL glass flask and stirred continuously at 60 rad s^{-1} for 20 min. Subsequently, 1.1 mL of 37% HCl was gently added to the precursor mixture with slow stirring. Following this, 150 mg of fine dry MXene powder was gradually introduced into the reaction mixture, and the flask was placed in an oil bath equipped with a temperature controller and magnetic stirrer. The reaction mixture was then heated at 68 °C for 5 h under the same stirring conditions. Once the process was complete, the solution was allowed to cool naturally to room temperature and then washed multiple times with a 1 : 1 distilled water/ethanol mixture by centrifugation at 7000 rpm for 5 min to remove any unbound MXene. Finally, the precipitated PB@MX NC was dried in a vacuum oven at 60 °C overnight, thus resulting in a fine powder for use in PD applications.

CVD graphene transfer and device fabrication

The graphene (Gr) monolayer was transferred *via* a polymer-assisted method. Briefly, a nitrocellulose layer was spin-coated onto the Gr/Cu sample, which was then immersed in the $FeCl_3$ etchant. After etching, the sample was rinsed three times in DI water and transferred onto the SiO_2/Si substrate with a 300 nm SiO_2 layer. The polymer layer was then removed using methanol, after which the Gr was washed several times in isopropanol and dried with argon gas. Further details on this procedure are provided in previous reports.[9,14,47]

For the device fabrication (Fig. S16†), a shadow mask was applied to the Gr monolayer on SiO_2/Si, after which the Au and Ti electrodes with thicknesses of 5 and 80 nm, respectively, were deposited using an e-beam evaporator.

Characterization

The NC morphology and chemical composition were examined by TEM (JEM-2100, JEOL, Japan) at an accelerating voltage of 200 kV, along with FE-SEM (JSM-7900F, JEOL, Japan) and EDS elemental mapping. The optical absorbance was measured using an ultraviolet-visible-near infrared (UV-Vis-NIR) optical spectrophotometer (DS104, Varian, UK). Raman spectroscopy of the graphene was conducted at room temperature using an in*Via* Renishaw Raman spectrometer with a 488 nm excitation wavelength at a power of 0.5 mW. A 600 nm grating and a 100× objective lens were used for the measurements. The emission spectra of the MX, PB, and *in situ* synthesized PB@MX NC were obtained using a Fluoromax-4 spectrofluorometer (Horiba Scientific, Japan) under 350 nm UV excitation. The surface static charge measurements of the MX and PB@MX NC coated on quartz substrates were investigated using a high-speed electrostatic voltmeter (TRek, model 370). The current–voltage measurements were performed using a Keithley 2461 source meter.

Data availability

The data supporting this article have been included as part of the ESI.†

Author contributions

A. G. was responsible for designing and conceptualizing the project, contributing to the methodology, and writing and reviewing the original draft. Y. J. R. and W. C. L. conducted a formal analysis and contributed to the experimental work. D. K. P. and C. T. L. analyzed the project and contributed to the methodology. I. K. and F. D. S. conducted formal analyses and contributed to the methodology. M. K. T., S. H. L., and Y. I. P. were involved in conceptualizing the project, providing direction and supervision, and in writing and reviewing the original draft.

Conflicts of interest

The authors declare no conflicts of interest.

Acknowledgements

A. G. and Y. I. P. are supported by the Basic Science Research Program through the National Research Foundation of Korea (NRF), funded by the Ministry of Education (2021R1I1A3047374 and RS-2023-00248654). S. H. L. acknowledges the support of the Global-Learning & Academic research institution for Masters', PhD students, and Postdocs (LAMP) Program of NRF grant funded by the Ministry of Education (RS-2024-00442775). M. K. T. and F. D. S. acknowledge the European Union's Horizon Europe research and innovation program under the Marie Sklodowska-Curie grant agreement no. 101152448 (INFRALIGHT). I. K. acknowledges the support of the European Union's Horizon 2020 European Research Council, under grant agreement no. 850875 (Light-DYNAMO). We would like to thank Yu-Jung Lu, Wei-Ren Syong, Jia-Zhu Zou, and Cheng-Hsueh Yang for their experimental help at an early stage of this work.

References

1 X. Huang, Y. Guo and Y. Liu, *Chem. Commun.*, 2021, **57**, 11429–11442.
2 J. Zhou, X. Liu, H. Zhou, S. Xu, J. Xie, C. Xu, W. Liu, Z. Zhang and C. Lee, *Laser Photonics Rev.*, 2025, **19**, 2400754.
3 A. Asaithambi, M. K. Thakur, D. Zhu, N. K. Tofighi, J. S. Pelli Cresi, S. Kuriyil, N. Curreli, N. Petrini, L. Rebecchi, L. De Trizio, A. Toma, L. Manna and I. Kriegel, *Adv. Funct. Mater.*, 2024, **34**, 2409951.
4 M. K. Thakur, A. Asaithambi, L. Rebecchi, S. Kuriyil and I. Kriegel, in *Emerging Materials for Energy and Sensing Applications*, CRC Press, Taylor & Francis Group, 2025, ISBN 9781032673691.
5 J. Han, W. Deng, F. Hu, S. Han, Z. Wang, Z. Fu, H. Zhou, H. Yu, J. Gou and J. Wang, *Adv. Funct. Mater.*, 2025, **35**, 2423360.
6 Z. Zhao, C. Xu, L. Niu, X. Zhang and F. Zhang, *Laser Photonics Rev.*, 2020, **14**, 2000262.
7 A. Gupta, S. Ghosh, M. K. Thakur, J. Zhou, K. K. Ostrikov, D. Jin and S. Chattopadhyay, *Prog. Mater. Sci.*, 2021, **121**, 100838.
8 A. Gupta, D. K. Patel, S. Y. Lee, A. F. Rigosi, R. E. Elmquist, V. N. K. B. Adusumalli, C.-T. Liang and Y. I. Park, *Adv. Funct. Mater.*, 2022, **32**, 2206496.
9 A. Gupta, M. K. Thakur, T. A. Effendi, R.-S. Chen, H.-Y. Cheng, K.-H. Lin, M. Bouras, D. S. Tomar, H. Y. Kuo and S. Chattopadhyay, *Chem. Eng. J.*, 2020, **420**, 127608.
10 B. Wang, S. Zhong, P. Xu and H. Zhang, *Chem. Eng. J.*, 2021, **403**, 126336.
11 D. Marpaung, J. Yao and J. Capmany, *Nat. Photonics*, 2019, **13**, 80–90.
12 L. Gao, Y. Zhao, X. Chang, J. Zhang, Y. Li, S. Wageh, O. A. Al-Hartomy, A. G. Al-Sehemi, H. Zhang and H. Ågren, *Mater. Today*, 2022, **61**, 169–190.
13 S. Ansari, S. Bianconi, C.-M. Kang and H. Mohseni, *Small Methods*, 2024, **8**, 2300595.
14 M. K. Thakur, A. Gupta, M. Y. Fakhri, R. S. Chen, C. T. Wu, K. H. Lin and S. Chattopadhyay, *Nanoscale*, 2019, **11**, 9716–9725.
15 S. Hegde, V. Sridhar, R. S. Chen and S. Chattopadhyay, *Adv. Opt. Mater.*, 2024, **12**, 2400232.
16 J. Yao, Z. Zheng, J. Shao and G. Yang, *Nanoscale*, 2015, **7**, 14974–14981.
17 O. Lopez-Sanchez, D. Lembke, M. Kayci, A. Radenovic and A. Kis, *Nat. Nanotechnol.*, 2013, **8**, 497–501.
18 L. Li and G. Shen, *Mater. Horiz.*, 2023, **10**, 5457–5473.
19 H. Xu, A. Ren, J. Wu and Z. Wang, *Adv. Funct. Mater.*, 2020, **30**, 2000907.
20 W. Deng, H. Huang, H. Jin, W. Li, X. Chu, D. Xiong, W. Yan, F. Chun, M. Xie and C. Luo, *Adv. Opt. Mater.*, 2019, **7**, 1801521.
21 J. Zou, Y. Huang, W. Wang, C. Li, S. Wei, H. Liu, L. Luo, W. Du, K. Shen and A. M. Ren, *ACS Appl. Mater. Interfaces*, 2022, **14**, 8243–8250.
22 J. Jeon, H. Choi, S. Choi, J. H. Park, B. H. Lee, E. Hwang and S. Lee, *Adv. Funct. Mater.*, 2019, **29**, 1905384.
23 J. Huang, J. Ding, F. Tan, Y. Gao, X. Lu, C. Dong, G. Yue, X. Xu and L. Ding, *J. Mater. Chem. C*, 2023, **11**, 17106–17114.
24 Z. Kang, Y. Ma, X. Tan, M. Zhu, Z. Zheng, N. Liu, L. Li, Z. Zou, X. Jiang and T. M. Zhai, *Adv. Electron. Mater.*, 2017, **3**, 1700165.
25 G. Prasad, S. A. Graham, J. S. Yu, H. Kim and D.-W. Lee, *Nano Energy*, 2023, **108**, 108178.
26 B. Kong, C. Selomulya, G. Zheng and D. Zhao, *Chem. Soc. Rev.*, 2015, **44**, 7997–8018.
27 M. Qiu, F. Zhou, P. Sun, X. Chen, C. Zhao and W. Mai, *Nano Energy*, 2020, **78**, 105148.
28 M. Qiu, P. Sun, Y. Liu, Q. Huang, C. Zhao, Z. Li and W. Mai, *Adv. Mater. Technol.*, 2018, **3**, 1700288.

29 F. S. Hegner, J. R. n. Galán-Mascarós and N. Lopez, *Inorg. Chem.*, 2016, **55**, 12851–12862.
30 S. Y. Lee, J.-Y. Park, H.-J. Kim, Y.-S. Lee and Y. I. Park, *J. Alloys Compd.*, 2022, **898**, 162952.
31 Y. Shi, G. Song, B. Yang, Y. Tang, Z. Liu, Z. Zhang, M. Shakouri, J. Cheng and H. Pang, *Adv. Mater.*, 2025, **37**, 2416665.
32 Z. Chen, Y. Wang, J. Wang, X. Li, G. Li, Z. Zhang, Z. Wu, X. Xie and N. Zhang, *Chem. Eng. J.*, 2025, **505**, 159519.
33 L. Guo, R. Mo, W. Shi, Y. Huang, Z. Y. Leong, M. Ding, F. Chen and H. Y. Yang, *Nanoscale*, 2017, **9**, 13305–13312.
34 Y. Li, X. Zhou, J. Wang, Q. Deng, M. Li, S. Du, Y.-H. Han, J. Lee and Q. Huang, *RSC Adv.*, 2017, **7**, 24698–24708.
35 D. Qu, Y. Jian, L. Guo, C. Su, N. Tang, X. Zhang, W. Hu, Z. Wang, Z. Zhao and P. Zhong, *Nano-Micro Lett.*, 2021, **13**, 1–13.
36 G. Kumar, A. Ahlawat, H. Bhardwaj, G. K. Sahu, P. S. Rana and P. R. Solanki, *Environ. Sci. Pollut. Res.*, 2024, **31**, 1–19.
37 A. Gupta, P. Gajula, J. U. Yoon, S. H. Lee, H. Kim, V. N. K. B. Adusumalli, J. W. Bae and Y. I. Park, *Nano Energy*, 2024, **122**, 109346.
38 A. Farah, C. Billing, C. Dikio, A. Dibofori-Orji, O. Oyedeji, D. Wankasi, F. Mtunzi and E. Dikio, *Int. J. Electrochem. Sci.*, 2013, **8**, 12132–12146.
39 L. Chang, S. Chang, W. Chen, W. Han, Z. Li, Z. Zhang, Y. Dai and D. Chen, *RSC Adv.*, 2016, **6**, 96223–96228.
40 Q. Luo, B. Chai, M. Xu and Q. Cai, *Appl. Phys. A*, 2018, **124**, 1–8.
41 J. Ran, G. Gao, F.-T. Li, T.-Y. Ma, A. Du and S.-Z. Qiao, *Nat. Commun.*, 2017, **8**, 13907.
42 M. Kataria, K. Yadav, G. Haider, Y. M. Liao, Y.-R. Liou, S.-Y. Cai, H.-i. Lin, Y. H. Chen, C. R. Paul Inbaraj, K. P. Bera, H. M. Lee, Y.-T. Chen, W.-H. Wang and Y. F. Chen, *ACS Photonics*, 2018, **5**, 2336–2347.
43 M. A. K. Purbayanto, S. W. Koh, F. Maddalena, D. Moszczyńska, J. Manopo, Y. Darma, D. Kowal, H. Li, M. D. Birowosuto and A. M. Jastrzębska, *Phys. Chem. Chem. Phys.*, 2023, **25**, 33081–33093.
44 J. A. Frank, H. Kalish, E. K. Jordan, S. A. Anderson, E. Pawelczyk and A. S. Arbab, *Mol. Imaging*, 2007, **6**, 7290.
45 M. Kataria, K. Yadav, S.-Y. Cai, Y.-M. Liao, H.-I. Lin, T. L. Shen, Y.-H. Chen, Y.-T. Chen, W.-H. Wang and Y.-F. Chen, *ACS Nano*, 2018, **12**, 9596–9607.
46 O. Leenaerts, B. Partoens, F. Peeters, A. Volodin and C. Van Haesendonck, *J. Phys.: Condens. Matter*, 2016, **29**, 035003.
47 T. Schultz, P. Bärmann, E. Longhi, R. Meena, Y. Geerts, Y. Gogotsi, S. Barlow, S. R. Marder, T. Petit and N. Koch, *Phys. Rev. Mater.*, 2023, **7**, 045002.
48 M. Khazaei, M. Arai, T. Sasaki, A. Ranjbar, Y. Liang and S. Yunoki, *Phys. Rev. B*, 2015, **92**, 075411.
49 M. K. Thakur, C.-Y. Fang, Y.-T. Yang, T. A. Effendi, P. K. Roy, R.-S. Chen, K. K. Ostrikov, W.-H. Chiang and S. Chattopadhyay, *ACS Appl. Mater. Interfaces*, 2020, **12**, 28550–28560.
50 M. Dave, P. V. Shah, N. Anuraag, N. Prasad, P. M. Pataniya and C. Sumesh, *Opt. Mater.*, 2024, **150**, 115244.
51 V. Selamneni, V. Adepu, H. Raghavan and P. Sahatiya, *FlatChem*, 2022, **33**, 100363.
52 L. Li, Y. He, T. Lin, H. Jiang, Y. Li, T. Lin, C. Zhou, G. Li and W. Wang, *Appl. Phys. Lett.*, 2024, **124**, 132105.
53 D. B. Velusamy, J. K. El-Demellawi, A. M. El-Zohry, A. Giugni, S. Lopatin, M. N. Hedhili, A. E. Mansour, E. D. Fabrizio, O. F. Mohammed and H. N. Alshareef, *Adv. Mater.*, 2019, **31**, 1807658.
54 X. Zhang, J. Shao, C. Yan, X. Wang, Y. Wang, Z. Lu, R. Qin, X. Huang, J. Tian and L. Zeng, *Mater. Des.*, 2021, **207**, 109850.
55 W. Song, Q. Liu, J. Chen, Z. Chen, X. He, Q. Zeng, S. Li, L. He, Z. Chen and X. Fang, *Small*, 2021, **17**, 2100439.
56 M.-Y. Li, Z. Li, H. Li, S. Liu, H. Lu, X. Wen and Y. Yang, *ACS Appl. Nano Mater.*, 2021, **4**, 13674–13682.
57 G. Luo, Z. Zhang, Y. Wang, Q. Deng, S. Pan, T. Wang, Q. Li, K. Liu, P. Kong and J. Zhang, *J. Mater. Sci. Technol.*, 2023, **156**, 83–91.
58 L. Luo, Y. Huang, K. Cheng, A. Alhassan, M. Alqahtani, L. Tang and Z. Wang, *Light: Sci. Appl.*, 2021, **10**, 177.
59 H. Guo, H. Wang, H. Fan, Q. Ye, J. Zhang, F. Cao, L. Li, Y. Tong and H. Wang, *Small*, 2021, **17**, 2101954.
60 N. Zhou, B. Xu, L. Gan, J. Zhang, J. Han and T. Zhai, *J. Mater. Chem. C*, 2017, **5**, 1591–1595.
61 A. Asaithambi, N. Kazemi Tofighi, N. Curreli, M. De Franco, A. Patra, N. Petrini, D. Baranov, L. Manna, F. D. Stasio and I. Kriegel, *Adv. Opt. Mater.*, 2022, **10**, 2200638.
62 J. K. El-Demellawi, S. Lopatin, J. Yin, O. F. Mohammed and H. N. Alshareef, *ACS Nano*, 2018, **12**, 8485–8493.
63 L.-B. Luo, L.-H. Zeng, C. Xie, Y.-Q. Yu, F.-X. Liang, C.-Y. Wu, L. Wang and J.-G. Hu, *Sci. Rep.*, 2014, **4**, 3914.
64 S. Wang, Y. Liu, Y. Liu and W. Hu, *Chem. Eng. J.*, 2023, **452**, 139512.